JOURNAL OF PROPULSION AND POWER
Vol. 18, No. 1, January–February 2002

Numerical Simulation of the Ram Accelerator Using a New Chemical Kinetics Mechanism

Michael J. Nusca*
U.S. Army Research Laboratory, Aberdeen Proving Ground, Maryland 21005

Computational fluid dynamics (CFD) solutions of the full Navier–Stokes equations, including finite-rate chemical kinetics, are used to numerically simulate the reacting in-bore flowfield for a 90-mm (bore diameter) ram-accelerator projectile propulsion system. In this system a gun tube is filled with a high-pressure gaseous mixture of hydrogen, oxygen, and nitrogen. An axisymmetric projectile is launched into this tube, and rails are attached to the tube wall to ensure projectile centering. The shock system that develops around the projectile, along with boundary layers on the projectile and tube surfaces, ignites the mixture on or near the projectile afterbody. The resulting pressure imbalance on the projectile generates thrust. Numerical predictions of this pressure field can be used to evaluate the thrust efficiency of the system, i.e., the projectile design combined with the chemical composition of the propellant gas. Comparison of the predicted pressure field and the measured pressure data is used to judge the accuracy of the CFD code. The choice of chemical kinetics mechanism used in the CFD code is of critical importance in achieving an accurate numerical simulation of the ram accelerator.

Nomenclature

C = concentration
C_f = forward rate constant, cm^3/mole-s
c_i = mass fraction of species i
c_p = specific heat capacity, constant p
c_v = specific heat capacity, constant volume
D_{ij} = diffusion coefficient, species i into j
D_{im} = diffusion coefficient, species i into mixture
E = Eckert number, V_∞^2/h_∞
E_f = dissociation energy
e = specific total internal energy
F, G = flux vectors [Eq. (1)]
g = Gibbs energy, $h - T\mathcal{S}$
H = source term vector [Eq. (1)]
h = molar specific enthalpy
k = Boltzmann's constant
k_f, k_b = forward, backward reaction rates [Eq. (15)]
k_T = thermal diffusion coefficient, D_T/D_{im}
L = reference length
Le = Lewis number, Pr/Sc
l_m = turbulence mixing length
M = Mach number or chemical third body
$\mathcal{M}$ = molecular weight
N = total number of species
Pr = Prandtl number, $\mu_\infty c_{p_\infty}/\kappa_\infty$
p = static pressure
q = heat transfer
$\Re_i$ = species i gas constant, $\bar{\Re}/\mathcal{M}_i$
$\bar{\Re}$ = universal gas constant
Re = Reynolds number, $\rho_\infty V_\infty L/\mu_\infty$
$\mathcal{S}$ = entropy
S_{ij} = computational cell area at i, j
Sc = Schmidt number, $\mu/\rho D$
T = temperature
t = time
U = dependent variable vector [Eq. (1)]
u = axial velocity component
V = magnitude of the local velocity vector
v = radial velocity component
$\dot{w}$ = chemical production term [Eq. (13)]
X = mole fraction
x, y = Cartesian coordinates
α = 0 for two-dimensional, 1 for axisymmetric flow
β = forward rate temperature exponent
Γ = $k_T\Lambda$
γ = ratio of specific heats, c_p/c_v
ΔH_f^o = enthalpy of formation
κ = thermal conductivity
Λ = $\mu Le/RePr$
μ = molecular viscosity
μ_t = turbulence viscosity
ν' = stoichiometric coefficient for reactants
ν'' = stoichiometric coefficient for products
ρ = density
σ = numerical dissipation coefficient
σ_{ij} = collision diameter, species i with j
σ_{xx} = normal stress tensor
σ_+ = axisymmetric stress tensor
τ_{xy} = shear stress tensor
Ω_D = collision integral for diffusion

Subscripts

i = ith species
i, j = mesh indicies
m = mixture
p = constant pressure
T = thermal quanity
v = constant volume
x, y = coordinates derivatives
wall = wall quantity
∞ = freestream quantity

Superscript

n = time level

Received 4 December 2000; revision received 15 June 2001; accepted for publication 20 July 2001.

*Aerospace Engineer, Weapons and Materials Research Directorate.

Introduction

THE ram accelerator is a gun-launch device used for accelerating projectiles to high velocity with a relatively low g loading. In this system a subcaliber projectile, typically a conical forebody attached to a reverse-cone afterbody, and full-bore obturator (i.e., backplate of full tube diameter) are injected at supersonic velocity

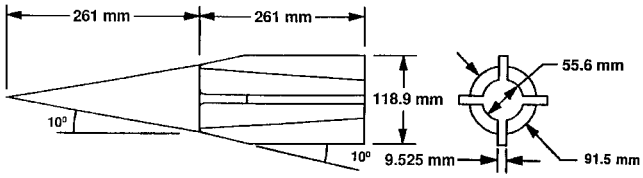

Fig. 1 Schematic of the ARL ramaccelerator system—smooth tube, finned projectile.

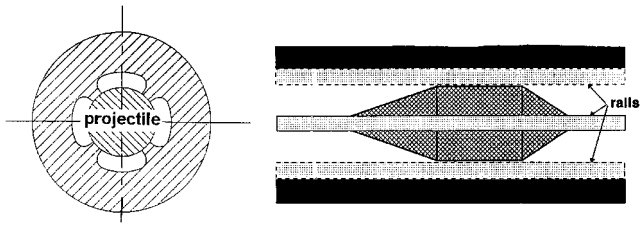

Fig. 2 Schematic of the ISL ramaccelerator system—railed tube, axisymmetric projectile.

into stationary tubes filled with pressurized mixtures of hydrocarbon, oxidizer, and inert gases. Flow stagnation on the obturator initiates combustion of the mixture, and then the obturator is gasdynamically discarded from the projectile. A system of shock waves generated around the projectile, in conjunction with viscous heating, sustains combustion. The resulting energy release, which travels with the projectile, also generates high pressures that impart thrust to the projectile.

Experimental testing and gasdynamic modeling of the ram accelerator has been carried out at the U.S. Army Research Laboratory (ARL) under the Hybrid Inbore RAM propulsion program.[1–4] This research program seeks to provide a highly efficient method of achieving hypervelocity ($\geq$3 km/s) projectile gun launch for use in high-speed impact testing applications. The ARL ram accelerator system used a 120-mm (bore diameter) tube, which was modeled after the 38-mm system at the University of Washington,[5] where the tube is of smooth bore and the projectile includes four to six fins to ensure projectile centering in the tube (see Fig. 1). Ram acceleration has also been demonstrated at the Institute of St. Louis (ISL) in France.[6,7] One of the ISL systems uses the smooth-bore tube and a finned projectile[6] and the other uses an axiymmetric projectile and a railed tube[7] to ensure projectile centering (see Fig. 2). Experimental data gathered in these facilities are available for use in validation of numerical simulations of the ram accelerator. In turn, these simulations assist the experimentalist in formulating an understanding of the physics of ram acceleration.

A number of numerical simulations have been generated for the ram accelerator, mainly for the smooth-bore/finned-projectile system, including those reported at the ARL; a comprehensive review is provided by Bruckner.[5] Numerical solutions of the Navier–Stokes equations have been obtained at the ARL via computational fluid dynamics (CFD) codes for nonreacting and reacting, two-dimensional (i.e., neglecting the projectile fins) and three-dimensional flows. These codes include models for chemically frozen (nonreacting) gas, finite-rate global and multiple step chemical kinetics, and equilibrium chemical processes.[3,8–16] Numerical simulation based on finite-rate chemical kinetics for hydrocarbon-based gases creates a very great demand on computational resources because the number of intermediate species and the number of kinetic steps for typical hydrocarbon fuels are prohibitively large. In addition, experimentally validated chemical kinetics mechanisms for the types of fuel-rich and high-pressure conditions prevalent in the ramaccelerator have not been available. Accordingly, CFD results from separate codes often yield very different results, even when attempting to simulate the same set of ram-accelerator data; a good review is provided by LeBlanc et al.[16]

Recently, a detailed hydrocarbon kinetics mechanism was developed by Petersen and Hanson at Stanford University, California.[17]

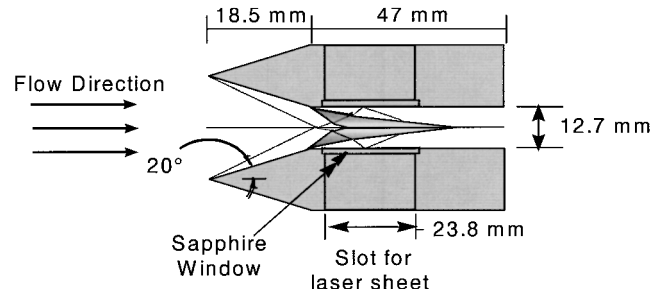

Fig. 3 Schematic of double-wedge/channel configuration (from Ref. 18).

This mechanism can be used to model finite-rate chemical reaction rates for gaseous mixtures of CH_4, H_2, O_2, and diluent at typical ramaccelerator conditions: pressures from 35 to 260 atm, temperatures from 1040 to 1600 K, and stoichiometric to fuel-rich (equilavence ratio $\geq$3) compositions. This mechanism was validated using shock-tube data.[17] The present paper discusses CFD simulations of the ram accelerator using this new chemical mechanism.

The following sections review the ARL reacting-flow model, the Stanford chemical kinetics mechanism, code validation using a test case, and finally simulations for the ram accelerator. The ARL CFD code is validated using a test case that is pertinent to propulsive flows involving combustion of hydrogen/oxygen/nitrogen in high-speed flow through a channel containing a double-wedge, i.e., flow through parallel plates with each plate consisting of a wedge-like surface as displayed in Fig. 3. Results of simultaneous schlieren/planar laser-induced fluorescence (PLIF) (for hydroxyl radical, OH) photography for the double-wedge/channel flow, produced at Stanford University,[18] reveal significant details in this flowfield. This test case has also been employed for CFD code validation by Choi et al.[19] For the present ram-accelerator simulations three-dimensional flow effects and multiple flow ignition sites caused by the projectile fins are eliminated by choosing the ISL's ramaccelerator configuration—axisymmetric projectile and railed tube (see Fig. 2). The rails on the tube wall are ignored, and the projectile is assumed to travel down the center of the tube thus allowing a two-dimensional simulation. Experimental pressure data, gathered using a multiple taps placed between the rails, provide data that are compatible with this scenario. In contrast, pressure data taken using taps placed along a smooth-bore tube can include the effects of masking by the fins on the projectile (see Fig. 1) as it slowly rotates in the tube. This situation would make comparison between computed and measured data difficult when the CFD simulation assumes a nonrotating projectile.

Reacting Flow Model

The chemically reacting hypervelocity flowfield around a body is numerically simulated using CFD. The NSRG2 code solves the two-dimensional/axisymmetric, unsteady, real-gas Navier–Stokes equations including equations for nonequilibrium chemical kinetics, chemical transport by diffusion, and heat transfer.[14,20–23] These partial differential equations are cast in conservation form and converted to algebraic equations using a finite volume formulation. Solution takes place on a mesh of nodes distributed in a zonal fashion throughout the flowfield such that sharp geometric corners and other details are accurately represented. The conservation law form of the equations ensures that the end states of regions of discontinuity (e.g., shocks) are physically correct even when smeared over a few computational cells.

The Navier–Stokes equations for two-dimensional/axisymmetric reacting (N species) and unsteady flow are written in the following conservation form. All variables have been nondimensionalized in a conventional fashion.[20,24]

$$\frac{\partial U}{\partial t} + \frac{\partial F}{\partial x} + \frac{\partial G}{\partial y} + H = 0 \tag{1}$$

$$U = \begin{pmatrix} \rho y^\alpha \\ \rho u y^\alpha \\ \rho v y^\alpha \\ \rho e y^\alpha \\ \rho c_1 y^\alpha \\ \vdots \\ \rho c_N y^\alpha \end{pmatrix}, \qquad F = \begin{pmatrix} \rho u y^\alpha \\ \left(\rho u^2 + \sigma_{xx}\right) y^\alpha \\ (\rho uv + \tau_{xy}) y^\alpha \\ (\rho ue + u\sigma_{xx} + v\tau_{yx} + q_x) y^\alpha \\ [\rho u c_1 - \Lambda(c_1)_x - \Gamma_1(\ell n T)_x] y^\alpha \\ \vdots \\ [\rho u c_N - \Lambda(c_N)_x - \Gamma_N(\ell n T)_x] y^\alpha \end{pmatrix}$$

$$H = \begin{pmatrix} 0 \\ 0 \\ \alpha\sigma_+ \\ 0 \\ -\dot{w}_1 y^\alpha \\ \vdots \\ -\dot{w}_N y^\alpha \end{pmatrix}$$

$$\sigma_{xx} = y^\alpha p + \frac{2\mu}{3y^\alpha Re}\left[\frac{\partial(y^\alpha u)}{\partial x} + \frac{\partial(y^\alpha v)}{\partial y}\right] - \frac{2\mu}{Re}\frac{\partial u}{\partial x}$$

$$\sigma_+ = p + \frac{2\mu}{3y^\alpha Re}\left[\frac{\partial(y^\alpha u)}{\partial x} + \frac{\partial(y^\alpha v)}{\partial y}\right] - \frac{2\mu}{Re}\frac{v}{y^\alpha}$$

$$\tau_{xy} = \tau_{yx} = \frac{2\mu}{3y^\alpha Re}\left(\frac{\partial u}{\partial y} + \frac{\partial v}{\partial x}\right)$$

$$q_x = -\frac{\kappa}{RePrE}\frac{\partial T}{\partial x} - \frac{\mu}{RePr}\sum_{i=1}^{N} Leh_i \frac{\partial c_i}{\partial x}$$

The G array is similar to the F array but contains y-derivative terms.[20] The ordinary diffusion coefficient D (see Le and Sc) is computed using Fick's law; diffusion components caused by concentration and thermal gradients (i.e., ∇c_i and $\nabla \ell n T$, respectively) are included (see definitions of Γ and Λ). The diffusive flux for species i is given by

$$\rho_i V_i = -\rho D_{\text{im}} \nabla c_i - \rho k_T D_{\text{im}} \nabla \ell n T \tag{2}$$

The thermal diffusion ratio k_T can be computed using semi-empirical formulations (see Refs. 20, 25, and 26 for details). The multicomponent diffusion coefficient D_{im} is given by Bird et al.[26] in terms of the species density ρ_i, velocity V_i, and mole fraction X_i, as well as the binary diffusion coefficient D_{ij}. In general, D_{im} depends on position in the flowfield, but for situations in which this dependence is slight $D_{\text{im}} \equiv D_{ij}$. For mixtures where component i diffuses into a mixture consisting of components $j = 2, N$ that move with the same velocity (or are stationary), an approximate formula can be used. This formula relates the binary diffusion coefficient for species i diffusing into species j, D_{ij}, to the multicomponent diffusion coefficient for species i diffusing into the mixture D_{im},

$$D_{\text{im}} = \frac{1 - X_i}{\sum_j X_j / D_{ij}} \tag{3}$$

The theory describing D_{ij} or diffusion in a binary gas mixture at low to moderate pressure is well developed. Solution of Boltzmann's equation and assuming an ideal-gas law results in the expression[27]

$$D_{ij} = \frac{0.00266 T^{\frac{3}{2}}}{p \mathcal{M}_{ij}^{\frac{1}{2}} \sigma_{ij}^2 \Omega_D} \tag{4}$$

where $\mathcal{M}_{ij} = 2[(1/\mathcal{M}_i) + (1/\mathcal{M}_j)]^{-1}$ is the combined molecular masses of species i and j. Rules used to obtain the interaction value σ_{ij} from σ_i and σ_j as well as Ω_D, which is related to the characteristic Lennard–Jones energy, are given by Reid et al.[27]

The species enthalpy per unit volume, mixture temperature, and specific heat are given by

$$h_i = e_i + \Re_i T \tag{5}$$

$$T = \frac{1}{c_v}\left[e - \frac{(u^2 + v^2)}{2} - \sum_{i=1}^{N} c_i \triangle H_{fi}^o\right] \tag{6}$$

$$c_v = \sum_{i=1}^{N} c_{v_i} c_i + \sum_{i=1}^{N} h_i \left(\frac{\partial c_i}{\partial T}\right)_v \tag{7}$$

(c_p similarly defined). The specific heat of each species (per mole) is given by the following polynomial[28] with coefficients $a_1 - a_7$:

$$c_{v_i} = \Re_i\left(a_1 T^{-2} + a_2 T^{-1} + a_3 + a_4 T + a_5 T^2 + a_6 T^3 + a_7 T^4\right) \tag{8}$$

with $c_{p_i} = c_{v_i} + \Re_i$. Equations (5–8) are solved iteratively for the mixture temperature. The Peng–Robinson equation of state[29] is used to determine pressure because gas pressure in the ram-accelerator system is very high (i.e., 50–500 atm).

$$p = \bar{\Re} T/(\bar{v} - b) - a/[\bar{v}(\bar{v} + b) + b(\bar{v} - b)] \tag{9}$$

$$a \equiv 0.45724\left(\bar{\Re}^2 T_c^2 / p_c\right)\left[1 + 0.37464\left(1 - T_r^{0.5}\right)\right]^2$$

$$b \equiv 0.0778(\bar{\Re} T_c / p_c) \tag{10}$$

where a is dependent on the critical temperature T_c and critical pressure p_c for the mixture. The mixture covolume is b, and $\bar{v}$ is the specific volume of the mixture (see Ref. 29).

The species viscosity μ_i and thermal conductivity κ_i can also be determined from curve-fit data. Coefficients $A_{\mu i} - D_{\mu i}$ and $A_{\kappa i} - D_{\kappa i}$ are given in Ref. 28.

$$\ell n(\mu_i) = A_{\mu i} \ell n(T) + B_{\mu i}/T + C_{\mu i}/T^2 + D_{\mu i} \tag{11}$$

$$\ell n(\kappa_i) = A_{\kappa i} \ell n(T) + B_{\kappa i}/T + C_{\kappa i}/T^2 + D_{\kappa i} \tag{12}$$

The mixture viscosity and thermal conductivity are determined using Wilke's law.[30] The mixture viscosity is then augmented by a turbulent component μ_t. The Cebeci–Smith turbulence model[31] is used to define μ_t.

Chemical reactions can be expressed in a general reaction equation given by (X_i represents the symbol for species i)

$$\sum_{i=1}^{N} \nu_i' X_{i\,k_b} \rightleftharpoons^{k_f} \sum_{i=1}^{N} \nu_i'' X_i \tag{13}$$

With a general reaction-rate equation given by

$$\frac{dC_i}{dt} = \frac{\dot{w}_i}{\mathcal{M}_i} = (\nu_i'' - \nu_i')\left(k_f \prod_i^N C_i^{\nu_i'} - k_b \prod_i^N C_i^{\nu_i''}\right) \tag{14}$$

The forward rates are specified

$$k_f = C_f T^\beta e^{-E_f/kT} \ (\text{cm}^3\ \text{mole}^{-1}\ \text{s}^{-1}) \tag{15}$$

while the backward rates are obtained from the equilibrium constant $K_{\text{eq}} = k_f/k_b$. Entropy $\mathcal{S}$ and enthalpy h are computed using curve fits,[28] and then for each reaction

$$K_{\text{eq}} = \exp(-\triangle g/\bar{\Re} T), \qquad \triangle g = g_{\text{products}} - g_{\text{reactants}}$$

$$g = h - T\mathcal{S} \tag{16}$$

Reaction-rate data for C_f, β, and E_f are discussed in the next section.

The integral form of the conservation equations [Eq. (1)] is convenient for the finite volume solution scheme:

$$\frac{\partial}{\partial t}\int_{\Omega}\int U\,\mathrm{d}x\,\mathrm{d}y + \int_{d\Omega} \boldsymbol{M}\cdot\hat{n}\,\mathrm{d}s + \int_{\Omega}\int H\,\mathrm{d}x\,\mathrm{d}y = 0 \quad (17)$$

where Ω is the region or computational cell, $d\Omega$ is the boundary or the cell sides, and $\hat{n}$ denotes the normal direction. The term $\boldsymbol{M} = F\hat{i}_x + G\hat{i}_y$ denotes the flux vector (second-order tensor), using unit vectors in each coordinate direction.

$$\frac{\partial}{\partial t}\int_{\Omega}\int U\,\mathrm{d}x\,\mathrm{d}y + \int_{d\Omega}(F\,\mathrm{d}y - G\,\mathrm{d}x) + \int_{\Omega}\int H\,\mathrm{d}x\,\mathrm{d}y = 0 \quad (18)$$

The semidiscrete form of Eq. (18) is given by

$$\frac{\mathrm{d}}{\mathrm{d}t}(S_{ij}U_{ij}) + LU_{ij} - DU_{ij} + S_{ij}H_{ij} = 0 \quad (19)$$

where LU_{ij} is the spatial discretization operator and DU_{ij} is the smoothing or dissipative operator. The effective flux through a cell face can be written as $LU_{ij} - DU_{ij}$. Four steps are used to determine the dependent variable array U [see Eq. (19)] for a cell centered at i, j, and time level $n+1$; the modified version of the classic Runge–Kutta scheme popularized by Jameson et al.[32] is chosen for the present work. The spatial discretization operator LU_{ij} is comprised of the flux terms F and G, which must be defined on the boundary of each cell. A combination of upwind differences and flux limiting is employed for this purpose.[20] The local stability bound for explicit schemes is defined using the Courant–Friedrichs–Lewy (CFL) number

$$\triangle t = \min\left(\triangle t_c, \frac{\mathrm{CFL}\cdot\triangle x}{|u|+a}, \frac{\mathrm{CFL}\cdot\triangle y}{|v|+a}\right) \quad (20)$$

where a is the local flow sound velocity. Because $\dot{w}_i$ can be assumed to remain nearly constant over a time step $\triangle t$, the chemical relaxation time step is given by

$$\triangle t_c = \triangle(\rho c_i)/\dot{w}_i \quad (21)$$

The CFL number can be specified as the same for all mesh cells and therefore $\triangle t$ can be different for each cell because $\triangle x$, $\triangle y$, u, v, and a can be different. Under this condition the solutions are not time accurate, but steady state can be achieved in fewer time steps. The mesh-constant CFL condition (local time stepping) acts like a preconditioner that reduces the numerical stiffness of the discrete system of equations arising from widely different mesh spacing and/or eigenvalues. For time-accurate simulations $\triangle t$ is constant over the entire mesh, and the CFL number is defined in terms of local flow conditions; for the modified Runge–Kutta scheme the CFL limit is $2\sqrt{2}$.

The present numerical solution scheme permits third-order odd-even decoupling throughout smooth regions of the flowfield and permits first-order oscillations near shocks. An appropriate smoothing formulation for this scheme, i.e., DU_{ij} term in Eq. (19), is one that is fourth-order throughout smooth regions of the flowfield and second-order near shocks. Jameson et al.[32] defined a dissipation operator that is a blend of second- and fourth-order smoothing with a pressure criterion; the pressure derivative acts as a "detector" for shock waves and gives the smoothing operator a second-order character (fourth order in smooth regions). However, rapid expansions, entropy singularities, and stagnation points can exhibit pressure gradients large enough to introduce second-order damping; it is not clear that these features require much damping to resolve them. An alternate scheme adds a final step to the Runge–Kutta time-marching scheme

$$U_{ij}^{n+1} = U_{ij}^{n+1} + \triangle U_{ij}^{(1)} + \triangle U_{ij}^{(2)} \quad (22)$$

$$\triangle U_{ij}^{(1)} = \sigma D_{xx}U_{ij}^{n+1}, \qquad \triangle U_{ij}^{(2)} = \sigma D_{yy}U_{ij}^{n+1} \quad (23)$$

where a single constant σ, chosen small enough to minimize numerical smearing of gradients and yield a unique and numerically stable solution (typically in the range of 0.0001 to 0.001), is used. The dissipation operators are undivided differences,

$$D_{xx}U_{ij}^{n+1} = (U_{i+1,j} - 2U_{ij} + U_{i-1,j})^{n+1}$$

$$D_{yy}U_{ij}^{n+1} = (U_{i,j+1} - 2U_{ij} + U_{i,j-1})^{n+1} \quad (24)$$

The terms σD_{xx} and σD_{yy} can be regarded as the artificial viscosity that has been added to the semidiscrete equation in order to damp oscillatory solutions. This form of the dissipation operator is second order. The central undivided differences for $\partial^2U/\partial x^2$ or $\partial^2U/\partial y^2$ act as the detectors for gradients of all conserved flow variables (i.e., are zero for no gradients and large for large gradients) and can be dropped for boundary layers (i.e., $\sigma = 0$), where artificial viscosity is not desired nor required. The added dissipation can reduce the accuracy of the solution locally to first order.

Chemical Kinetics Mechanism

A detailed hydrocarbon kinetics mechanism was developed by Petersen and Hanson[17] using the shock-tube facility at Stanford University. This mechanism can be used to model shock-tube ignition delay times for $CH_4/H_2/O_2/D$ gases (D as a diluent only, e.g., N_2, He) at pressures from 35 to 260 atm, temperatures from 1040 to 1600 K, and stoichiometric to fuel-rich (equivalence ratio ≥ 3) compositions. The new detailed mechanism called RAMEC (38 species and 190 reactions) produces chemical ignition delay times that agree well with the shock-tube data. Comparisons of the Chapman–Jouget detonation velocity using the RAMEC mechanism and theoretical values are very encouraging.[17] Petersen and Hanson[17] have also produced a skeletal mechanism REDRAM (22 species and 34 reactions) that essentially reproduces the shock-tube data and results of the detailed mechanism RAMEC. In addition, a $H_2/O_2/D$ kinetics mechanism (D as a diluent only, e.g., N_2, He) that forms a subset of the REDRAM mechanism is used in the present study. Table 1 lists this mechanism and rate data (M is a third body). The rates for reactions 11, 13, and 14, are more complex.[17] Collision efficiencies for reactions involving M are given in Ref. 17.

Alternatives to the REDRAM chemical kinetics mechanism for $H_2/O_2/N_2$ are that of Jachimowski (20 reactions and eight species when N and NO are dropped from the original H_2-air mechanism)[33] and a modified-Jachimowski mechanism.[34] The Jachimowski mechanism accounts for all reactions given in Table 1 (albeit with different rate parameters and third-body collision efficiencies) along with five additional reactions: $H_2 + O_2 \rightarrow 2OH$, $HO_2 + H \rightarrow H_2O + O$, $HO_2 + O \rightarrow O_2 + OH$, $HO_2 + OH \rightarrow H_2O + O_2$, and $O + H_2O_2 \rightarrow OH + HO_2$. The modified-Jachimowski mechanism excludes the

Table 1 REDRAM kinetics mechanism (from Ref. 17)

Number	Reaction	C_f	β	E_f/k
1	$O + H_2 \leftrightarrow H + OH$	5.0×10^4	2.7	3165.6
2	$H + O_2 + M \leftrightarrow HO_2 + M$	2.8×10^{18}	−0.9	0.0
3	$H + O_2 + O_2 \leftrightarrow HO_2 + O_2$	3.0×10^{20}	−1.7	0.0
4	$H + O_2 + H_2O \leftrightarrow HO_2 + H_2O$	9.38×10^{18}	−0.8	0.0
5	$H + O_2 + N_2 \leftrightarrow HO_2 + N_2$	2.6×10^{19}	−1.2	0.0
6	$H + O_2 \leftrightarrow O + OH$	8.3×10^{13}	0.0	7253.7
7	$H + HO_2 \leftrightarrow O_2 + H_2$	2.8×10^{13}	0.0	537.5
8	$H + HO_2 \leftrightarrow OH + OH$	1.34×10^{14}	0.0	319.6
9	$H + H_2O_2 \leftrightarrow HO_2 + H_2$	1.21×10^7	2.0	2617.0
10	$OH + H_2 \leftrightarrow H_2O + H$	2.16×10^8	1.5	1726.2
11	$OH + OH + M \leftrightarrow H_2O_2 + M$	7.4×10^{13}	−0.4	0.0
12	$OH + HO_2 \leftrightarrow O_2 + H_2O$	2.9×10^{13}	0.0	−251.6
13	$OH + H_2O_2 \leftrightarrow HO_2 + H_2O$	1.75×10^{12}	0.0	161.0
14	$HO_2 + HO_2 \leftrightarrow O_2 + H_2O_2$	1.3×10^{11}	0.0	−820.3
15	$O + O + M \leftrightarrow O_2 + M$	1.2×10^{17}	−1.0	0.0
16	$O + H + M \leftrightarrow OH + M$	5.0×10^{17}	−1.0	0.0
17	$H + OH + M \leftrightarrow H_2O + M$	2.2×10^{22}	−2.0	0.0
18	$H + H + M \leftrightarrow H_2 + M$	1.0×10^{18}	−1.0	0.0

reaction $H_2 + O_2 \rightarrow 2OH$ and reverses the reaction $HO_2 + H \rightarrow H_2 + O_2$ (uses reverse reaction rate).

Results for Test Case

Experimental Results

Stanford has embarked on an experimental investigation of the shock-wave structure and combustion fronts around blunt bodies and wedge geometries similar to the ram accelerator. One such geometry is the double-wedge/channel shown schematically in Fig. 3. This model was mounted in the test section of an expansion tube described by Morris et al.[18] The test gas mixture was $2H_2 + O_2 + mN_2$ ($m = 12$ or 17; $m = 12$ was used for the present study), and the freestream flow conditions for the channel were 2130 m/s, 0.12 atm, 290 K, for velocity, pressure, and temperature, respectively. The freestream Mach number and Reynolds number are 5.8 million and 1.4×10^6 per meter, respectively.

Figure 4 shows photographs that combine schlieren images with PLIF images of OH, for the double-wedge channel flow. These images were produced at Stanford.[18] The leading-edge shocks emanating from the wedges and shock interaction at the centerplane are recognized as typical schlieren features. Areas of combustion (i.e., presence of significant OH) in the wall boundary layers and centerplane shear layer are shown as bright white regions residing between the delimiters of the PLIF sheet. The PLIF image of the OH species was taken for a restricted length along the channel (see Fig. 3); the absence of a white-glow superimposed on the schlieren image in a region that is out of the PLIF field of view does not necessarily indicate an absence of OH in the flowfield. For example, it is expected that OH is present upstream of the PLIF field of view in the shock layers and boundary layers on the wedge surfaces.

Computational Grid and Boundary Conditions

Figure 5 shows the shock/shear-layer adapted computational grid consisting of 106 cells in the streamwise direction and 75 cells in the stream-normal direction (chosen after further grid-refinement demonstrated results that were essentially grid independent). The figure displays only half of the actual number of grid cells, for clarity. The grid is adapted to the leading-edge shocks and concentrates more cells near the channel centerplane. Solid wall surfaces are prescribed with no-slip, isothermal, noncatalytic boundary conditions. For noncatalytic walls the surface-normal gradients of the species mass fractions are zero. The channel inflow is supersonic as is the outflow (with minor corrections to account for the channel wall boundary layers). The small upper and lower grid sections upstream of the wedge surfaces are treated as lines of symmetry.

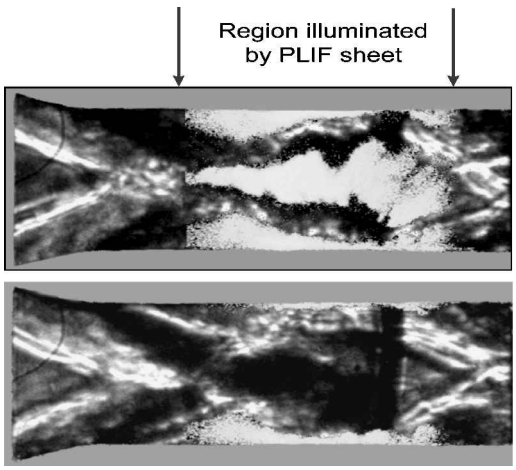

Fig. 4 Simultaneous schlerien/PLIF (OH species) for double-wedge/channel test case (from Ref. 18). Upper view for $2H_2 + O_2 + 12N_2$ mixture. Lower view for $2H_2 + O_2 + 17N_2$ mixture.

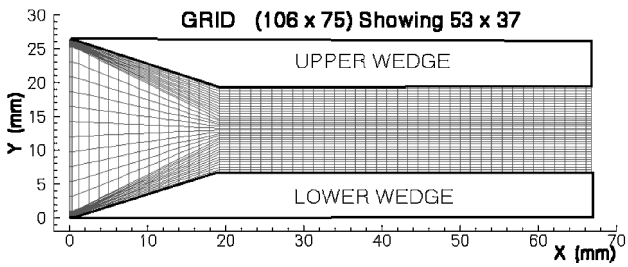

Fig. 5 Computational grid for the double-wedge/channel test case.

Computational Results

Figure 6 shows the computed density field displayed as grey-scale flood/line contours. Comparing Fig. 6 with the schlieren images of Fig. 4, it is encouraging to see a good correlation with the locations of leading-edge shock intersections (at about 20 mm) and the downstream intersection of reflected shocks (at about 50 mm). Figure 7 shows the computed OH mass fraction field displayed as grey-scale flood contours. In each case the location of the PLIF image (from Figs. 3 and 4) is overlayed for reference. Because of significant flow heating in the shock layers near the wedge surfaces, OH is readily formed in these regions. Flow expansion from the wedge surfaces onto the channel walls causes a local thickening of the boundary layers; subsequently shocks reflected onto the channel walls cause a local thinning of the boundary layers. These flow features can be recognized by a distinctive "bump" in the wall distribution of OH mass fraction located at about 84 mm. The lack of significant OH formation at the channel centerline (compare Figs. 4 and 7) can be the results of 1) incomplete flow mixing caused by inadequate turbulence modeling, 2) inaccurate chemical kinetics rates for low gas temperatures, or 3) inadequate grid resolution. Grid refinement was not found to improve the results. Neither alternative turbulence models nor improved kinetics rates were implemented in the present study. Because Choi et al.[19] observed combustion at the centerline to be a highly transient event, resolution of this issue was delayed pending further investigation.

The solution was checked for grid independence by doubling the number of grid cells in each direction and verifying that the same results were acheived. Additional computations using the chemical kinetics mechanism of Jachimowski[33] and a modified-Jachimowski mechanism[34] were performed. Although the modified-Jachimowski mechanism produced OH mass fraction distributions that were very similar to those achieved using the REDRAM (Table 1) mechanism, results using the Jachimowski mechanism were quite different. In

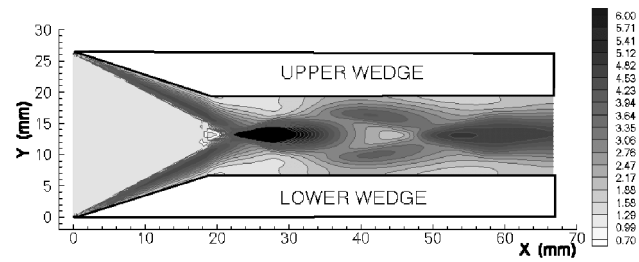

Fig. 6 Nondimensional density (ρ/ρ_∞) contours for the double-wedge/channel test case.

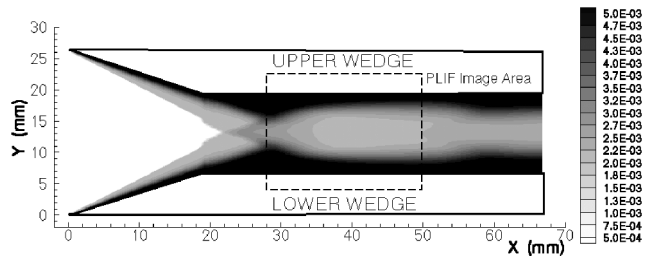

Fig. 7 Mass fraction contours (OH) for the double-wedge/channel test case.

the latter case OH concentrations remained high throughout the channel after the leading-edge shocks with little structure (unlike the structured OH distributions shown in Fig. 7).

Results for the Ram Accelerator

Computational Grid and Boundary Conditions

Figure 8 shows the computational grid used for the ram-accelerator simulations. There are 314 grid cells in the axial direction and 40 grid cells in the radial direction (chosen after further grid refinement demonstrated results that were essentially grid independent). The figure shows every other grid cell. The grid is essentially uniform in each direction with some radial grid clustering near the tube wall and the projectile surface wall. The wall grid spacing is approximately 0.07 mm, which is considered more than adequate for inviscid flow simulations and satisfactory for viscous flow simulations (the turbulence model follows a law-of-the-wall methodology). All dimensions follow those used in the ISL ram accelerator (Fig. 2). The projectile nose tip is pointed as is the projectile base. A grid region that is 4 mm long was placed in front of the projectile nosetip and 10 mm were placed behind the projectile base.

The inflow is prescribed in accordance with the conditions of Shot 222 of the ISL (see Refs. 7 and 35). The outflow is assumed supersonic for inviscid flow simulations with boundary condition corrections applied for viscous simulations in the thin boundary-layer region on the tube wall and the projectile wake region near the tube centerline. The wall boundary conditions are no penetration for inviscid and no slip for viscous simulations with isothermal and noncatalytic conditions imposed as well. Computations are done in the projectile-fixed reference frame assuming a constant flow velocity (i.e., the inflow and the tube wall are assumed to be moving at the prescribed projectile velocity). As a direct result, a boundary layer will not form on the tube wall until the projectile's bow shock reflects from it (for viscous flow simulations). The small sections of tube centerline ahead of and behind the projectile are treated as lines of symmetry.

Computational Results

Figures 9–11 show results for the inviscid, inert flowfield. The projectile bow shock reflects from the tube wall at about 70 mm

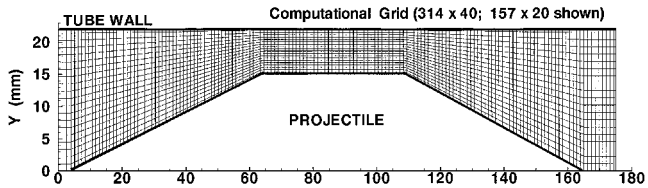

Fig. 8 Computational grid for the ISL ramaccelerator configuration.

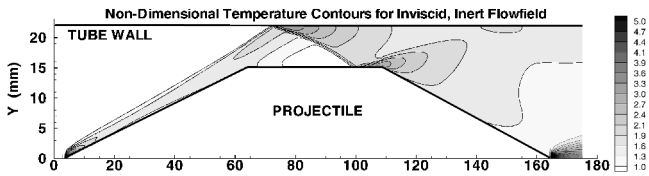

Fig. 9 Nondimensional temperature (T/T_∞) contours for inviscid, nonreacting flow conditions.

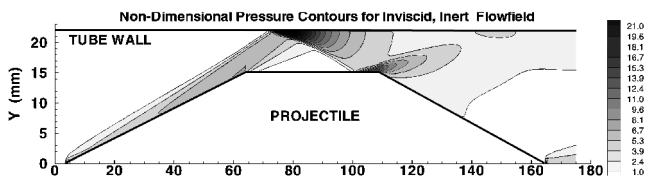

Fig. 10 Nondimensional pressure (p/p_∞) contours for inviscid, nonreacting flow conditions.

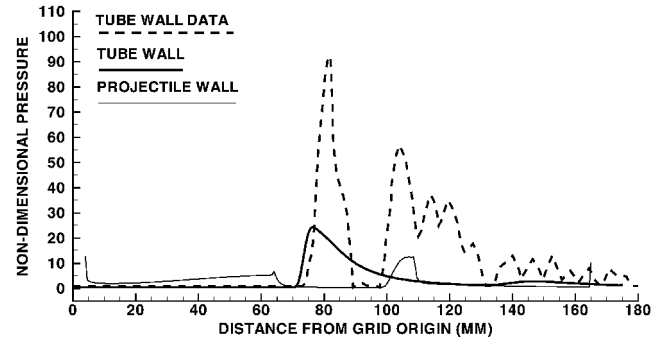

Fig. 11 Nondimensional pressure (p/p_∞) distributions along tube wall and projectile wall for inviscid, nonreacting flow conditions. Comparison with measured pressure data.

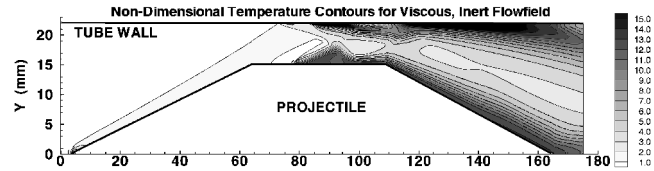

Fig. 12 Nondimensional temperature (T/T_∞) contours for viscous, nonreacting flow conditions.

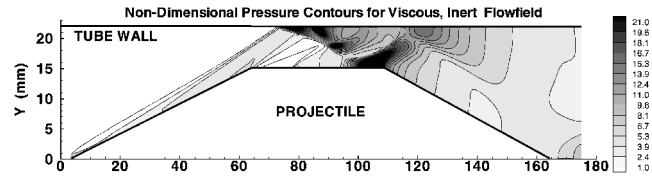

Fig. 13 Nondimensional pressure (p/p_∞) contours for viscous, nonreacting flow conditions.

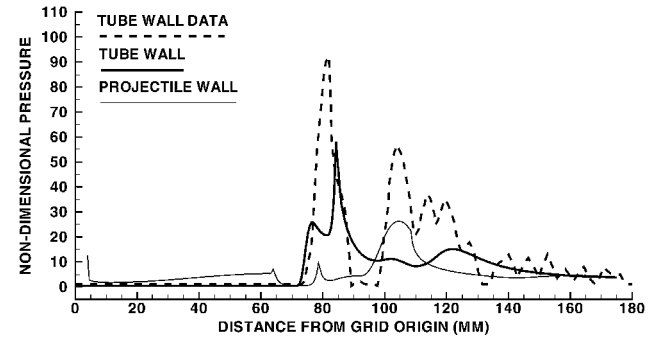

Fig. 14 Nondimensional pressure (p/p_∞) distributions along tube wall and projectile wall for viscous, nonreacting flow conditions. Comparison with measured pressure data.

from the grid origin as indicated by a sharp rise in temperature (Fig. 9) and pressure (Figs. 10 and 11) at this point. Pressure is nearly constant on the projectile forebody and decreases in the flow expansion onto the midbody (Fig. 11). The bow shock reflection is slightly curved as a result of its interaction with the expansion wave generated at the projectile forebody-midbody junction and intersects the projectile near the end of the midbody (Figs. 9 and 10). Note the pressure rise on the projectile surface at about 100–110 mm (Fig. 11). This shock reflects again and is severely weakened in the expanding afterbody flowfield. It intersects the tube wall at about 150 mm (note the small pressure rise in Fig. 11 at this location). A strong recompression is noted at the projectile base along the axis (Figs. 9–11). The computed pressure distribution is not in agreement with the tube wall data (Fig. 11) because these data were taken in the reactive flow environment.

Figures 12–14 show results for the viscous, inert flowfield. Laminar boundary layers are permitted to naturally form on the

tube wall and the projectile walls. Note the thick regions of higher temperature on the walls in Fig. 12. The boundary layer on the projectile forebody is very thin and does not cause noticeable changes to the pressure and temperature fields as compared to the inviscid results. Observations of laminar boundary-layer thickening on the projectile midbody surface, after the flow expansion, prompted the choice to let the boundary layer become turbulent at the axial location of about 75 mm (see Fig. 14). For consistency, this location was also used on the tube wall (i.e., about 5 mm downstream of the bow-shock reflection point). For both surfaces the transition to turbulence causes a small shock to form (Figs. 12 and 13) as indicated by a pressure increases on both walls at about 80 mm (see Fig. 14). As for the inviscid flowfield, the projectile bow shock reflects from the tube wall at about 70 mm from the grid origin as indicated by a sharp rise in temperature (Fig. 12) and pressure (Figs. 13 and 14) at this point. The bow-shock reflection is more highly curved (Fig. 13) because of its interaction with the expansion wave generated at the projectile forebody-midbody junction and the small shocks generated on the body and on the tube at the location of boundary-layer transition. The resultant shock intersects the projectile farther from the end of the midbody (Figs. 12 and 13). Note the larger pressure rise on the projectile surface at about 105 mm (Fig. 14). This shock reflects again and is weakened in the expanding afterbody flowfield (Fig. 13). It intersects the tube wall at about 120 mm (note the pressure rise in Fig. 14 at this location). A strong recompression does not occur at the projectile base along the axis (as is the case with inviscid flow; see Fig. 10) because of the thick boundary layer from the projectile afterbody (Fig. 12). The computed pressure distribution is in better agreement with the tube wall data (Fig. 14) as compared to the inviscid result (Fig. 11). The double-pressure spike computed between 70 and 90 mm begins to approach the measured pressure levels. Smaller computed pressure increases at 102 and 120 mm seem to mimic the pressure data trends at these locations.

Figures 15–17 show pressure results for the viscous, reacting flowfield. Comparing Fig. 13 (viscous, inert flow) and Fig. 15 (the contours have been purposely plotted using the same limits), one can observe regions of high pressure on the tube wall in a generally similar pattern or distribution. The same can be said for the projectile surface except that on the afterbody (110–165 mm) the pressures are not only higher for reacting flow but the distribution is not as characteristic of simple flow expansion. Rather, the afterbody pressures for reacting flow are more concentrated on the surface because of the heat release of combustion. Figure 16 shows

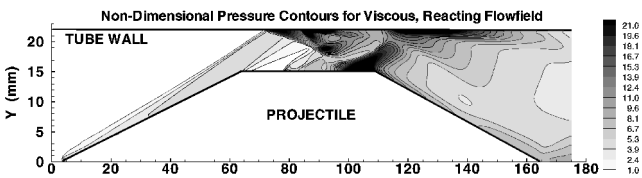

Fig. 15 Nondimensional pressure (p/p_∞) contours for viscous, reacting flow conditions.

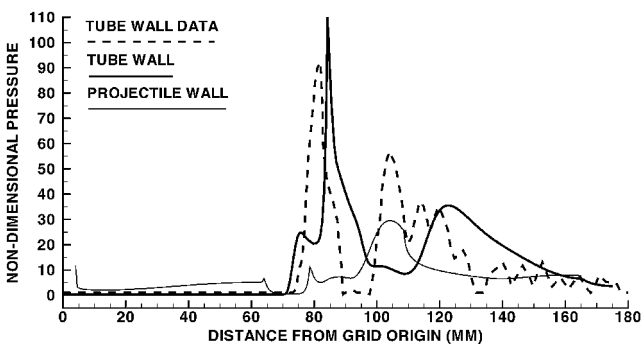

Fig. 16 Nondimensional pressure (p/p_∞) distributions along tube wall and projectile wall for viscous, reacting flow conditions. Comparison with measured pressure data.

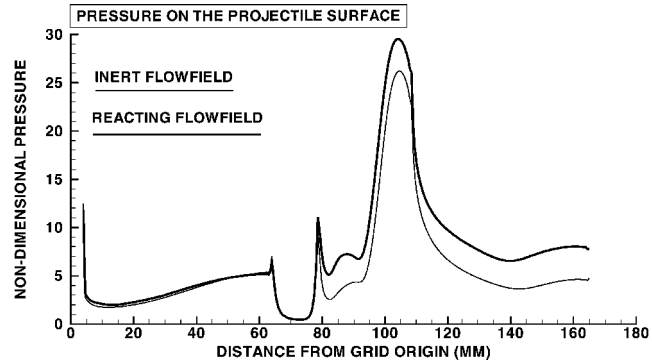

Fig. 17 Nondimensional pressure (p/p_∞) distributions along projectile wall for both nonreacting and reacting, viscous flow conditions.

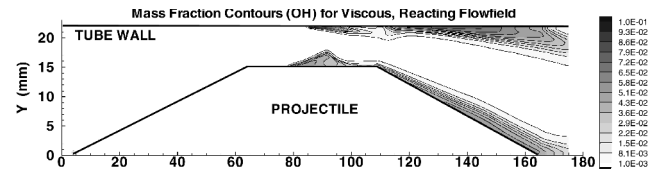

Fig. 18 Mass fraction (OH) contours for viscous, reacting flow conditions.

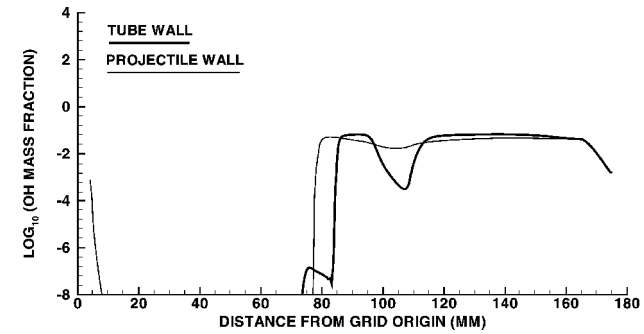

Fig. 19 Mass fraction (OH) distributions along tube wall and projectile wall for viscous, reacting flow conditions.

the pressure distributions, and Fig. 17 compares the projectile surface pressure distributions for inert and reacting flow. Comparing Fig. 14 (viscous, inert flow) and Fig. 16 (the pressure axis has been purposely plotted using the same limits), one can observe a very similar pressure rise between 70 and 75 mm (as a result of the reflection of the projectile's bow shock on the tube wall) and a marked increase in pressures on the tube wall after that point. This is because of combustion. Note the similarities between computed and measured tube wall pressures, displayed in Fig. 16, with the exception of the region near 105 mm. Here we see a measured pressure rise to about 60 with no corresponding computed pressure peak; the computations do show a comparable pressure rise at 120 mm on the tube wall (more will be said about this below). Figure 17 highlights the computed increase in pressure on the projectile surface as a result of combustion. In particular, the reacting flow, relative to the inert flow, shows very slight increases in pressures on the forebody, where the projectile generates a drag force, but marked increase in pressure on the afterbody (>110 mm) where the projectile generates thrust. Note in Fig. 17 that the forebody and afterbody pressure are nearly the same for inert flow but that the afterbody pressure is notably higher than the forebody pressure for the reactive flow. This is of course where the ram-accelerator concept provides its propulsive mechanism.

Figures 18 and 19 show the computed mass fraction contours and surface distributions for the specie OH. The OH radical (along with the H_2O molecule) is noteworthy because it is formed during heat release in H_2/O_2 combustion. Plotted results for H_2O are qualitatively

similar those of OH (other species such as HO_2 and H_2O_2 form behind the projectile's bow shock and subsequent shocks reflected from the tube wall to the projectile). Very small levels of OH are observed on the projectile forebody with significant concentrations found in the hot wall boundary layers. The mass fraction of OH in the space between the projectile and tube walls is smaller than 0.001. The qualitative pattern of the OH contours, seen in Fig. 18, is strikingly similar to that photographed in the Stanford University expansion tube (Fig. 3) and computed using the ARL CFD code (Fig. 7).

For Fig. 19 the levels of OH on the projectile surface and on the tube wall are similar except for a significant reduction in OH on the tube wall between 95 and 115 mm. The cause of this reduction is unclear without further investigation, but the associated reduction in heat release causes a lower then expected pressure in this region (see Fig. 16).

There has been some evidence presented by Seiler et al.[35] that the projectile surface participates in the chemical ignition process of the flowfield, sustained combustion results for an aluminum and a titanium projectile, but not for a steel projectile. The computations were repeated using a fully catalytic boundary surface condition on the projectile. The wall is said to be fully catalytic if the chemical reactions are catalyzed at an infinite rate, i.e., the mass fractions of the species are at their local equilibrium values at the local pressure and temperature at the wall. These results are generally indistinguishable from those acheived with noncatalytic walls. Closer examination reveals that even though the wall values of OH and other product species are different (e.g., equilibrium mass fraction of OH on the projectile wall is smaller by about a factor of two) the net effect on flowfield properties far from the walls is small. It can be postulated that aluminum and titanium, when used in the construction of the projectile, provide a catalytic and/or ignition effect, which allows shock/boundary-layer flow heating to complete the combustion process. The Stanford chemical kinetic mechanism, used in the ARL CFD simulations, does not model this wall catalysis effect. However, the model proves useful in achieving a good comparison with measured results for those cases in which sustained combustion was observed in the experimental firing.

Conclusions

Computational fluid dynamics solutions of the full Navier–Stokes equations, including finite-rate chemical kinetics, are used to numerically simulate the reacting in-bore flowfield for a 90-mm ram-accelerator projectile propulsion system. The shock system that develops around the projectile along with boundary layers on the projectile and tube surfaces ignites the mixture on or near the projectile afterbody. Examinations of the computed pressure distribution on the projectile shows that the forebody and afterbody pressure are nearly the same for inert flow but that the afterbody pressure is notably higher that the forebody pressure for the reactive flow. This is of course where the ram-accelerator concept provides its propulsive mechanism. Comparison of the predicted pressure field and the measured pressure data shows that the CFD code, coupled with the chemical kinetics mechanism, is able to resolve most of the details in the ram-accelerator flowfield.

Acknowledgments

This work was supported by the U.S. Army Research Laboratory, the U.S. Department of Defense High Performance Computing Research Initiative, and the ARL Major Shared Resource Center. Computer time on the NAVO and CEWES Cray computers is also greatly appreciated.

References

[1]Kruczynski, D. L., Liberatore, F., and Nusca, M. J., "Experimental Flow Visualization for a Large-Scale Ram Accelerator," *Journal of Propulsion and Power*, Vol. 12, No. 1, 1996, pp. 206–210.

[2]Kruczynski, D. K., "High Performance Ram Accelerator Research," *Ram Accelerators*, edited by K. Takayama and A. Sasoh, Springer-Verlag, Berlin, 1998, pp. 97–104.

[3]Nusca, M. J., and Kruczynski, D. L., "Reacting Flow Simulation for a Large-Scale Ram Accelerator," *Journal of Propulsion and Power*, Vol. 12, No. 1, 1996, pp. 61–69.

[4]Nusca, M. J., "Numerical Simulation of Unsteady Ram Accelerator Flow Phenomena," *Ram Accelerators*, edited by K. Takayama and A. Sasoh, Springer-Verlag, Berlin, 1998, pp. 305–312.

[5]Bruckner, A. P., "The Ram Accelerator: Overview and State of the Art," *Ram Accelerators*, edited by K. Takayama and A. Sasoh, Springer-Verlag, Berlin, 1998, pp. 3–24.

[6]Giraud, M., Legendre, J. F., and Henner, M., "RAMAC in Subdetonative Propulsion Mode: State of the ISL Studies," *Ram Accelerators*, edited by K. Takayama and A. Sasoh, Springer-Verlag, Berlin, 1998, pp. 65–77.

[7]Seiler, F., Patz, G., Smeets, G., and Srulijes, J., "Presentation of the Rail Tube Version II of ISL's RAMAC 30," *Ram Accelerators*, edited by K. Takayama and A. Sasoh, Springer-Verlag, Berlin, 1998, pp. 79–88.

[8]Nusca, M. J., "Numerical Simulation of Reacting Flow in a Thermally Choked Ram Accelerator Projectile Launch System," AIAA Paper 91-2490, July 1991; see also U.S. Army Ballistic Research Lab., BRL-TR-3222, Aberdeen Proving Ground, MD, April 1991.

[9]Kruczynski, D. L., and Nusca, M. J., "Experimental and Computational Investigation of Scaling Phenomena in a Large Caliber Ram Accelerator," AIAA Paper 92-3245, July 1992.

[10]Nusca, M. J., "Numerical Simulation of Fluid Dynamics with Finite-Rate and Equilibrium Combustion Kinetics for the 120-MM Ram Accelerator," AIAA Paper 93-2182, June 1993.

[11]Nusca, M. J., "Reacting Flow Simulation for a Large Scale Ram Accelerator," AIAA Paper 94-2963, July 1994.

[12]Nusca, M. J., "Reacting Flow Simulation of Transient Multi-Stage Ram Accelerator Operation and Design Studies," AIAA Paper 95-2494, July 1995.

[13]Nusca, M. J., "Investigation of Ram Accelerator Flows for High Pressure Mixtures of Various Chemical Compositions," AIAA Paper 96-2946, July 1996.

[14]Nusca, M. J., "Computational Simulation of the Ram Accelerator Using a Coupled CFD/Interior-Ballistics Approach," AIAA Paper 97-2653, July 1997.

[15]Nusca, M. J., "Computational Simulation of Starting Dynamics in a Ram Accelerator," AIAA Paper 98-3146, July 1998.

[16]LeBlanc, J. E., Nusca, M. J., Wang, X., Seiler, F., Sugihara, M., and Fujiwara, T., "Numerical Simulation of the Ramac Benchmark Test," *Proceedings of the Fourth International Workshop on Ram Accelerators*, Univ. of Poitiers, Poitiers, France, Sept. 1999, pp. 101–131; see also *Proceedings of the 17th International Colloquium on the Dynamics of Explosive and Reactive Systems*, Heidelberg, Germany, July 1999, pp. 69–99.

[17]Petersen, E., and Hanson, R., "Reduced Kinetics Mechanisms for Ram Accelerator Combustion," *Journal of Propulsion and Power*, Vol. 15, No. 4, 1999, pp. 591–600; see also "Experimental Investigation of Ram Accelerator Flowfields and Combustion Kinetics," *Ram Accelerators*, edited by K. Takayama and A. Sasoh, Springer-Verlag, Berlin, 1998, pp. 281–294.

[18]Morris, C. I., Kamel, M. R., and Hanson, R. K., "Expansion Tube Investigation of Ram-Accelerator Projectile Flowfields," AIAA Paper 96-2680, 1996; see also "Experimental Investigation of Ram Accelerator Flowfields and Combustion Kinetics," *Ram Accelerators*, edited by K. Takayama and A. Sasoh, Springer-Verlag, Berlin, 1998, pp. 281–294.

[19]Choi, J. Y., Jeung, I. S., and Yoon, Y., "Unsteady Simulation of Model Ram Accelerator in Expansion Tube," AIAA Paper 98-3450, 1998; see also "Numerical Investigation of Ram Accelerator Flow Field in Expansion Tube," *Ram Accelerators*, edited by K. Takayama and A. Sasohv, Springer-Verlag, Berlin, 1998, pp. 312–323.

[20]Nusca, M. J., "Numerical Simulation of Electromagnetic Wave Attenuation in Nonequilibrium Chemically Reacting Flows," *Computers and Fluids*, Vol. 27, No. 2, 1998, pp. 217–238.

[21]Nusca, M. J., Dinavhai, S. P. G., and Soni, B., "Grid Adaption Studies for Reactive Flow Modeling of Propulsion Systems," AIAA Paper 99-0970, Jan. 1999.

[22]Nusca, M. J., McQuaid, M. J., and Anderson, W. R., "Investigation of a High-Velocity, Multi-Species Jet Undergoing Unsteady Expansion into Open-Air," AIAA Paper 2000-0819, Jan. 2000.

[23]Nusca, M. J., Miziolek, A. W., and Rosocha, L. A., "Numerical Studies of NO_x Reduction in a Non-Thermal Plasma Channel-Flow Reactor," AIAA Paper 2000-0719, Jan. 2000.

[24]Widhopf, G. F., and Wang, J. C. T., "A TVD Finite-Volume Technique for Nonequilibrium Chemically Reacting Flows," AIAA Paper 88-2711, June 1988.

[25]Chapman, S., and Cowling, T., *The Mathematical Theory of Non-Uniform Gases*, Cambridge Univ. Press, Cambridge, England, UK, 1970, pp. 155, 165.

[26]Bird, R., Stewart, W., and Lightfoot, E., *Transport Phenomena*, Wiley, New York, 1960, p. 571.

[27]Reid, R., Prausnitz, J., and Poling B., *The Properties of Gases and Liquids*, 4th ed., McGraw–Hill, New York, 1987, pp. 581–589.

[28]McBride, B. J., and Gordon, S., "Computer Program for Calculation of Complex Chemical Equilibrium Compositions and Applications, II. Users Manual and Program Description," NASA RP 1311, June 1996, Appendix E.

[29]Benedek, P., and Olti, F., *Computer Aided Chemical Thermodynamics of Gases and Liquids*, Wiley, New York, 1985, pp. 107–114.

[30]Wilke, C. R., "A Viscosity Equation for Gas Mixtures," *The Journal of Chemical Physics*, Vol. 18, No. 4, 1950, pp. 517–519.

[31]Smith, A. M. O., and Cebeci, T., "Numerical Solution of the Turbulent Boundary-Layer Equations," Douglas Aircraft Div., Rept. DAC 33735, April 1967.

[32]Jameson, A., Schmidt, W., and Turkel, E., "Numerical Simulation of the Euler Equations by Finite Volume Methods Using Runge–Kutta Time Stepping Schemes," AIAA Paper 81-1259, June 1981.

[33]Jachimowski, C. J., "An Analytical Study of the Hydrogen-Air Reaction Mechanism with Application to Scramjet Combustion," NASA TP 2791, May 1988.

[34]Matsuo, A., and Fujii, K., "Examination of the Improved Model for the Unsteady Combustion Around Hypersonic Projectiles," AIAA Paper 95-2565, July 1995.

[35]Seiler, F., Patz, G., Smeets, G., and Srulijes, J., "Influence of Projectile Material and Gas Composition on Superdetonative Combustion in ISL's RAMAC 30," AIAA Paper 98-3445, July 1998.